CHEMISTRY OF MATERIALS

pubs.acs.org/cm

Article

Ambient Synthesis of Pt-Reactive Metal Alloy and High-Entropy Alloy Nanocatalysts Utilizing Hydrogen Cold Plasma

Dezhen Wu, Libo Yao, Michael Ricci, Jialu Li, Rongxuan Xie, and Zhenmeng Peng*

Cite This: *Chem. Mater.* 2022, 34, 266−272

Read Online

ACCESS | Metrics & More | Article Recommendations | Supporting Information

ABSTRACT: Synthesis of platinum-reactive metal alloy (Pt-RMA) and its high-entropy alloy (Pt-HEA) nanoparticles is challenging due to the huge difference in reduction potentials between Pt and reactive metal precursors and the oxyphilic nature of reactive metals. Herein, we utilize hydrogen cold plasma to synthesize a variety of Pt-RMA (Pt−Cr, Pt−Ta, Pt−V, Pt−Fe, and Pt−Al) and Pt-HEA (Pt−Cr−Ta−V−Fe−Al) nanoparticles under ambient conditions. Effectiveness of the method is attributed to the generation of hydrogen anions in hydrogen plasma, possessing extremely strong reducing ability with its −2.3 V standard reduction potential that can simultaneously reduce Pt and reactive metal precursors. The synthesized nanoparticles are characterized for confirming the alloy formation and are studied for the catalytic properties in the methanol oxidation reaction, with improved activity and durability compared to commercial Pt. This study provides an effective, universal method to synthesize Pt-RMA and Pt-HEA nanoparticles, which offers a new platform for studying this group of nanomaterials.

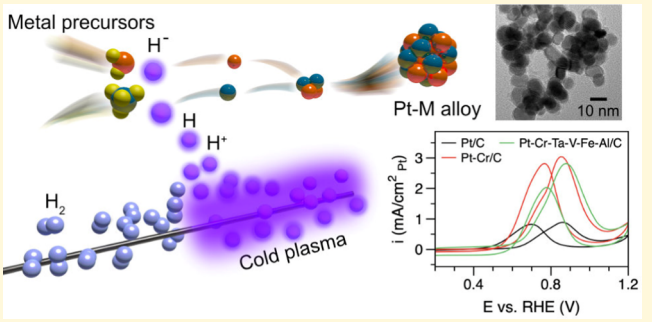

INTRODUCTION

It has been discovered that the catalytic properties of metal materials can be dramatically altered by alloying with different elements. Platinum alloy nanomaterials, in particular, have attracted intensive research for decades owing to their interesting catalytic properties and important applications in many chemical and electrochemical reactions.[1−3] For instance, Pt-based alloy nanoparticles remain the most active catalysts in a range of reactions such as methanol oxidation reaction (MOR), hydrogen evolution reaction, and oxygen reduction reaction.[4−8] A major research focus in this field is to discover new advanced Pt alloys to further improve the catalytic properties. However, previous studies focused primarily on alloys of Pt with metals that can be easily reduced.[6,9,10] Alloys of Pt with reactive metals, including early transition metals and main group metals that are extremely susceptible to oxidation, were rarely studied, despite the fact that they represent a large group of materials and would potentially exhibit interesting catalytic properties as discovered in most recent studies.[11−13]

The lack of study of Pt-reactive metal alloys (Pt-RMAs) is mainly caused by the difficulty in material synthesis. Because reactive metals have rather negative reduction potentials, for instance, −1.18 V for V^{2+}/V and −1.66 V for Al^{3+}/Al versus +1.18 V for Pt^{2+}/Pt, reduction of their precursors becomes challenging with conventional synthesis methods. For example, the most commonly used reducing reagent, hydrogen gas, appeared to be ineffective in the thermal reduction of Pt-RMAs even with the reduction temperature approaching as high as one thousand degrees Celsius, which can be attributed to insufficient reducing power of hydrogen molecules (0 V for H^+/H_2). Moreover, with the drastic difference in their standard reduction potentials between Pt and RMs, this method often leads to prioritized Pt reduction that generates multiple phases instead of uniform Pt-RMAs.[14,15] Another approach using extremely strong reducing reagents, such as alkali metals (e.g., −2.71 V for Na^+/Na), has been demonstrated with the synthesis of Pt-RMAs. However, it requires very cautious handling with more reactive chemicals.[16−18] The physical metallurgical strategy, such as sputtering and gas aggregation methods, provides an alternative route for obtaining Pt-RMAs. Nonetheless, this approach, with typical extreme operation condition requirements and low capability of scaled preparation of Pt-RMA nanomaterials, is primarily limited to fundamental studies.[19−22] To fully exploit the promise of Pt-RMAs for catalytic properties and real-world applications, a novel synthesis method that can generate these nanomaterials more efficiently is required.

In this work, we report a new, hydrogen cold plasma-enabled synthesis method for rapid and facile preparation of Pt-RMA nanoparticles under ambient conditions. This new approach

Received: September 30, 2021
Revised: December 16, 2021
Published: December 29, 2021

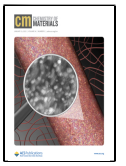

https://doi.org/10.1021/acs.chemmater.1c03389
Chem. Mater. 2022, 34, 266−272

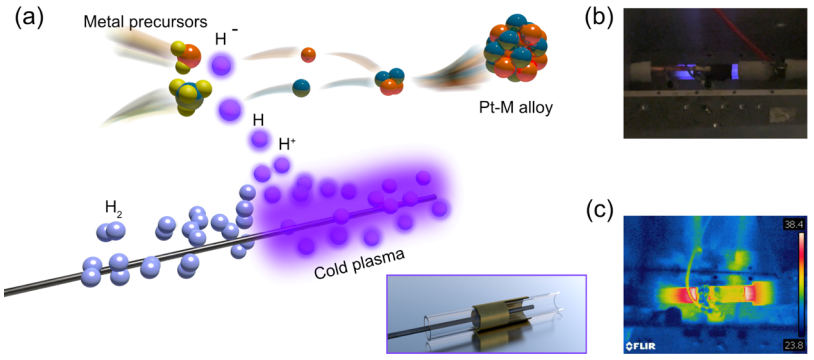

Figure 1. (a) Schematic illustration of hydrogen cold plasma synthesis of Pt-RMA and Pt-HEA nanoparticles, with the inset figure showing a DBD reactor. (b) Plasma generator in operation, emitting glowing H_2 cold plasma. (c) Infrared thermal image of the DBD reactor taken after 10 s of operation.

utilizes in situ-generated hydrogen cold plasma that consists of energetically activated species including hydrogen anions (H^-), hydrogen radicals ($H^\bullet$), and excited hydrogen molecules (H_2*).[23−26] Particularly, H^- has a low standard reduction potential of −2.3 V, which is more negative than that of many RMs and thus can simultaneously reduce Pt and RMs for their alloy formation. A variety of Pt-RMA nanoparticles, including Pt−Cr, Pt−Ta, Pt−V, Pt−Fe, and Pt−Al, are synthesized within minutes, proving rapid, facile, and effective features of this method. Hydrogen cold plasma-enabled synthesis of Pt-high entropy alloys (Pt-HEAs), another important category of materials with interesting properties, is also demonstrated with a Pt−Ct−Ta−V−Fe−Al alloy, suggesting its robust and universal capability and potential of this new method to be applied in Pt-RMA and Pt-HEA research.

RESULTS AND DISCUSSION

Figure 1 illustrates the hydrogen cold plasma synthesis process of Pt-RMA nanoparticles. In a typical synthesis, a Pt precursor and a reactive metal precursor were well-mixed and loaded into a dielectric barrier discharge (DBD) reactor (Figure 1, inset). The reactor was purged by argon for the removal of air and moisture prior to the experiment, for the purpose of eliminating oxygen-containing species that would lead to reaction with RMs. Hydrogen gas was thereafter fed to the reactor for its cold plasma generation at room temperature and atmospheric pressure. Experimentally, the reduction process became complete within only 10 min of reaction. Figure S1a,b shows the experimental setup and DBD reactor parameters. Figure 1b,c shows the cold plasma synthesis in process, with purple illuminance being observed as a result of hydrogen plasma generation, and the reactor temperature increased from room temperature to about 40 °C in about 10 s and further ramped and stabilized at around 200 °C with elongated reaction time. Previous investigations have discovered that a variety of active species, including $H^\bullet$, H^-, and H_2*, would be produced in hydrogen plasma and possess strong reducing power.[23−25] These active species would likely follow a trend of $H^- > H^\bullet > H_2$* in terms of reducing power, considering that the same element in a lower valence typically possesses a stronger reducing capability. Recently, a few studies reported the utilization of hydrogen plasma for synthesis of late transition-metal nanoparticles.[27−30] Although these studies focused on late transition metals, which are significantly easier to reduce than reactive metals, the successful nanoparticle synthesis under ambient conditions provides evidence for the strong reducing capability of hydrogen plasma. In particular, the in situ-generated H^- species has a standard reduction potential of −2.3 V versus SHE, which is dramatically lower in comparison with that of Pt and all studied reactive metals in this work (Figure 2), representing an extremely strong

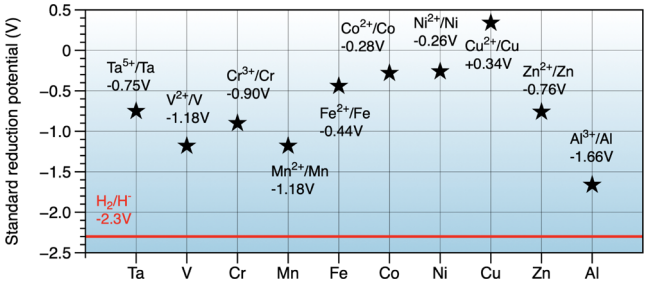

Figure 2. Standard reduction potentials of H-, Ta, V, Cr, Fe, Al, and some typical transition metal ions.

reductant that can effectively reduce these Pt-RMAs. It would be possible that H radicals and active H_2* also participated in the reduction process, considering that they have more negative reduction potentials compared to that of Pt. From the thermodynamic point of view, the low standard reduction potential of H anions provides the driving force for Pt-RMA reduction. From the kinetic point of view, thanks to the high reducing capability of the hydrogen plasma and its near zero activation time, the cationic metal precursors can be reduced to zero-valent metal atoms instantly and simultaneously. The abundance of metal atoms in close proximity leads to a burst nucleation followed by random metal atom deposition, which results in the uniform atomic mixing of different metal elements and their growth into nanoparticles.[31,32] Thus, the huge difference in the reduction potentials makes the reduction of these metal precursors thermodynamically favorable and kinetically fast, leading to Pt-RMA formation.

The effectiveness and universality of the hydrogen cold plasma synthesis method were investigated with Pt−Cr, Pt−Ta, Pt−V, Pt−Fe, and Pt−Al systems. The metal precursors exhibit a color change immediately after applying the hydrogen plasma (Figure S2), indicating a rapid reduction process. All the obtained products are found in the form of spherical nanoparticles with transmission electron microscopy (TEM) characterizations (Figures S3−S7). Carbon support was not used in the synthesis to avoid electrical arcs.[33,34] Consequently,

https://doi.org/10.1021/acs.chemmater.1c03389
Chem. Mater. 2022, 34, 266−272

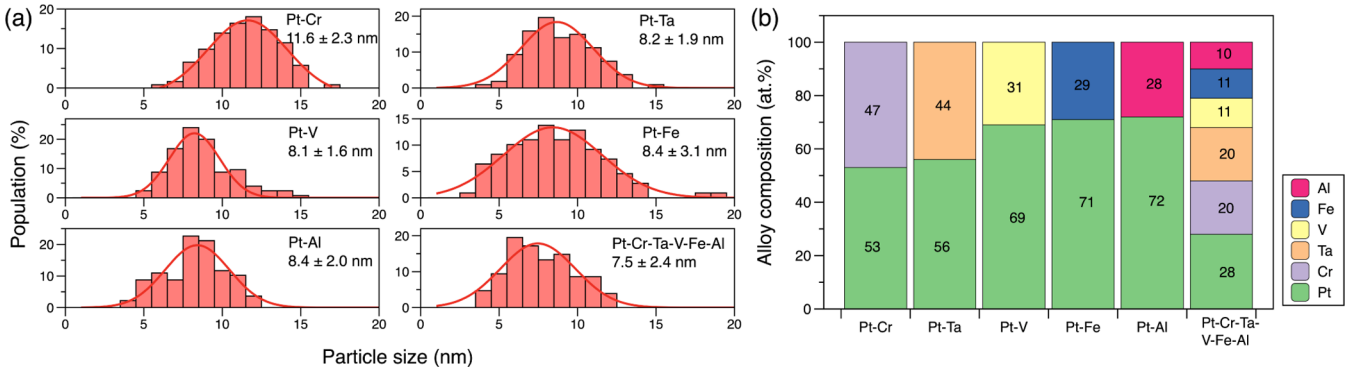

Figure 3. (a) Particle size distribution and calculated Gaussian curves of Pt−Cr, Pt−Ta, Pt−V, Pt−Fe, Pt−Al, and Pt−Cr−Ta−V−Fe−Al alloys. A hundred particles were counted for each sample for size distribution analysis. (b) Alloy composition of synthesized alloys from SEM−EDX characterization.

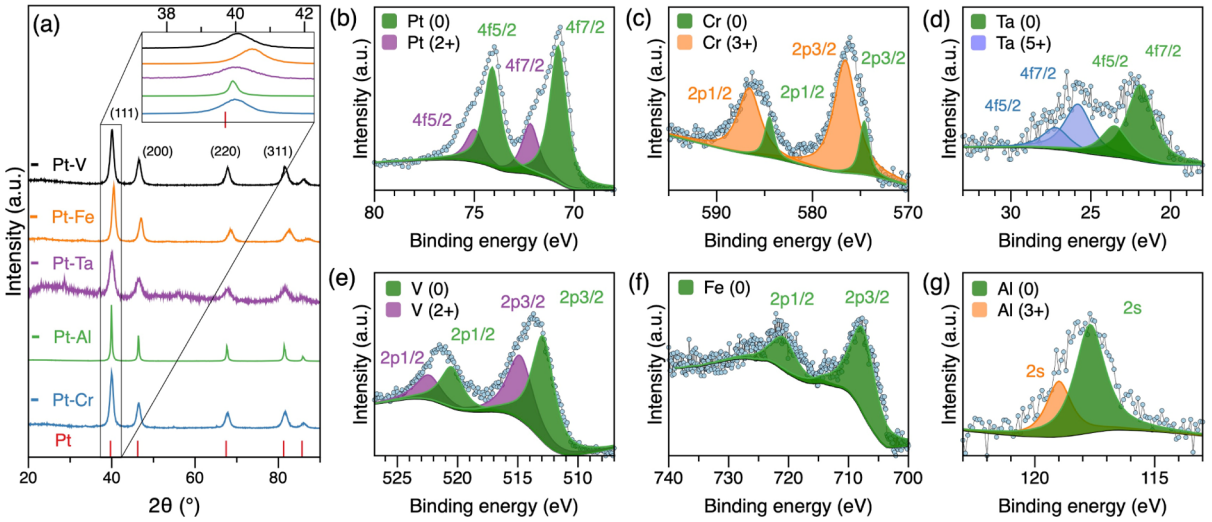

Figure 4. (a) XRD patterns of the as-synthesized Pt−Cr, Pt−Al, Pt−Ta, Pt−Fe, and Pt−V nanoparticles (Inset figure: enlargement of their (111) diffraction peaks showing significant shifts relative to that of pure Pt); (b−g) Representative XPS spectra of Pt 4f in Pt−Cr, Cr 2p in Pt−Cr, Ta 4f in Pt−Ta, V 2p in Pt−V, Fe 2p in Pt−Fe, and Al 2s in Pt−Al, with the spectra deconvoluted into peaks attributed to the metallic and oxidative valence states.

the produced nanoparticles suffered from a mild agglomeration without the support, which can be circumvented by applying a nonconductive supporting material. The average particle size is measured to be 11.6 ± 2.3, 8.2 ± 1.9, 8.1 ± 1.6, 8.4 ± 3.1, and 8.4 ± 2.0 nm for the as-synthesized Pt−Cr, Pt−Ta, Pt−V, Pt−Fe, and Pt−Al, respectively (Figure 3a). Additionally, nanoparticle size can be tuned by changing the power input of the plasma generator. Pt−Cr nanoparticles with 5.5, 9.9, and 12.7 nm particle size were obtained with a plasma input of 60, 90, and 120 W (Figure S8). Energy-dispersive X-ray (EDX) quantitative analyses determine overall particle compositions of $Pt_{53}Cr_{47}$, $Pt_{56}Ta_{44}$, $Pt_{69}V_{31}$, $Pt_{71}Fe_{29}$, and $Pt_{72}Al_{28}$ in these products (Figures 3b and S9−S13). The composition of these synthesized Pt-RMA nanoparticles can be tuned by controlling the amounts of Pt and RM precursors during synthesis (Figure S14). X-ray diffraction (XRD) characterization confirms a pure face-centered cubic (fcc) phase, with the characteristic peaks indexed to {1 1 1}, {2 0 0}, {2 2 0}, and {3 1 1} planes (Figure 4a). All five samples exhibit significant peak shifts toward a higher angle compared to that of pure Pt (JCPDS no. 04-0836), indicating the formation of alloys. Moreover, metal oxides of any kind were not observed in the XRD spectra, suggesting the single phase of the alloys. The crystallite size for $Pt_{53}Cr_{47}$, $Pt_{56}Ta_{44}$, $Pt_{69}V_{31}$, $Pt_{71}Fe_{29}$, and $Pt_{72}Al_{28}$ was estimated using the Scherrer equation to be 8.7, 7.5, 7.8, 8.2, and 8.3 nm, which is consistent with the measured size from microscopy images. The alloy formation is further evidenced with X-ray photoelectron spectroscopy (XPS) characterizations. Figure 4b,c shows representative Pt 4f and Cr 2p XPS spectra of $Pt_{53}Cr_{47}$ nanoparticles. Both elements are found with significant content in the metallic state, confirming that they are effectively reduced by the hydrogen cold plasma and form an alloy.[35] The $Pt_{56}Ta_{44}$, $Pt_{69}V_{31}$, $Pt_{71}Fe_{29}$, and $Pt_{72}Al_{28}$ samples also show clear metallic states and thus provide additional evidence for their alloy formation (Figure 4d−g). It is worth noting that the signals of these elements in their oxidative state can also be observed in the XPS spectra, which can be attributed to surface oxidation after being exposed to the air atmosphere due to the oxyphilic nature of reactive metals.[36−38] The valance states of Pt and reactive metals before and after the hydrogen cold plasma treatment are compared in Figure S15, which show obvious peak shifts toward a lower binding energy (i.e., a lower valance state). The synthesis reaction time effect was investigated (Figure S16), with a complete reduction in the Pt-RMAs within about 10 min. These results confirm

https://doi.org/10.1021/acs.chemmater.1c03389
Chem. Mater. 2022, 34, 266−272

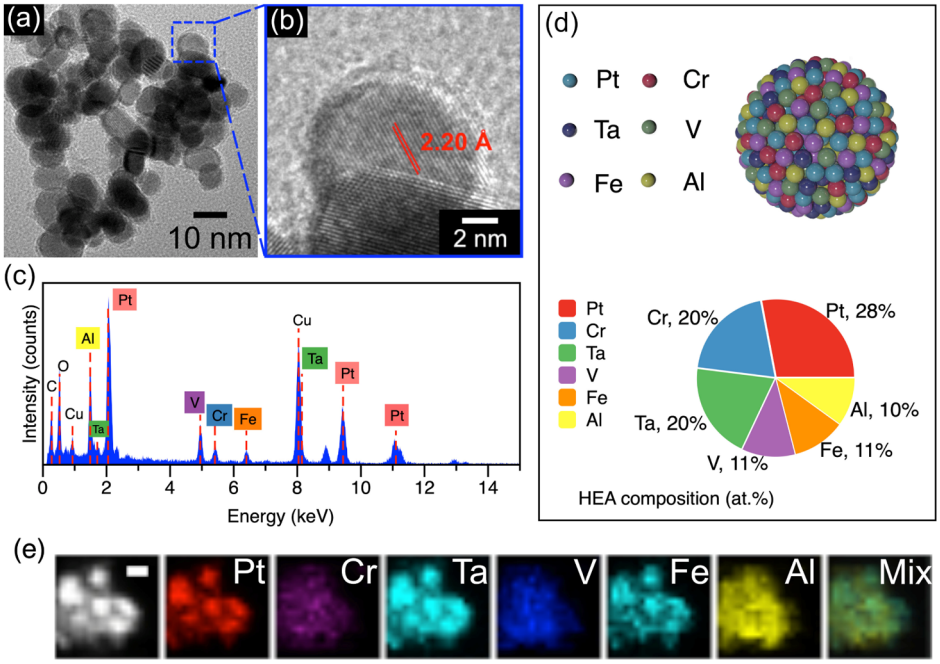

Figure 5. (a) TEM, (b) HRTEM, and (c) EDX spectrum, (d) EDX quantitative analysis of the as-synthesized Pt−Cr−Ta−V−Fe−Al alloy nanoparticles, and (e) STEM imaging and elemental mapping of Pt, Cr, Ta, V, Fe, and Al in the selected area. The scale bar in the STEM image represents 5 nm.

that the hydrogen cold plasma method can be used for effective synthesis of Pt-RMA nanoparticles.

This new method was also investigated for the synthesis of Pt-HEA nanoparticles. The Pt−Cr−Ta−V−Fe−Al senary alloy was produced by mixing all six metal precursors and reducing them using the hydrogen cold plasma, following a similar procedure as for Pt-RMA synthesis. The product consists of uniform nanoparticles with an average size of 7.5 ± 2.4 nm (Figures 5a and S17) and exhibits a single fcc phase in structure (Figure S18). Clear lattice fringes are observed on the high-resolution TEM (HRTEM) image, with a measured 2.2 Å *d*-spacing assigned to the {1 1 1} plane (Figure 5b). The *d*-spacing value measurement in combination with the observed positive shift of the diffraction peaks as shown on the XRD pattern indicates a lattice contraction as a result of the alloy formation.[35,39] Figure 5c shows the EDX spectrum of the nanoparticles, which contains all six elements and determines an overall composition of $Pt_{28}Cr_{20}Ta_{20}V_{11}Fe_{11}Al_{10}$ (Figures 5d and S19). Careful characterizations of individual nanoparticles with scanning TEM (STEM) and EDX elemental mapping find a uniform distribution of the six elements throughout the particles with no significant phase separation (Figure 5e). XPS verifies the presence of metallic states of all six elements in the nanoparticles (Figure S20). These characterizations collectively confirm the successful synthesis of Pt−Cr−Ta−V−Fe−Al Pt-HEA nanoparticles.

The catalytic properties of Pt-RMA and Pt-HEA nanoparticles in MOR were investigated by loading the synthesized nanoparticles onto the carbon support (50 wt %) and conducting electrochemical measurements, including all seven catalyst materials and commercial Pt/C for comparison (Figure S21). Figure 6a shows cyclic voltammetry (CV) curves of the Pt−Cr/C and Pt−Cr−Ta−V−Fe−Al/C, as representative Pt-RMA and Pt-HEA nanoparticle catalysts, and commercial Pt/C (20 wt %) in the N_2-protected 0.1 M $HClO_4$ electrolyte. The Pt−Cr/C and Pt−Cr−Ta−V−Fe−Al/C show a smaller double-layer capacitance compared to the Pt/C, which can be attributed to their different metal loadings and thus different surface areas for capacitive charging and discharging. Both catalysts exhibit characteristic features associated with hydrogen underpotential deposition (H_{UPD}), indicating the presence of Pt atoms on the catalyst surface. The significantly weaker H_{UPD} signals compared to the Pt/C suggest fewer Pt surface atoms in these alloy catalysts, which can be attributed to their bigger particle size and lower Pt content. The MOR area-specific activity, which represents the intrinsic property of a catalyst, was evaluated by testing the catalyst materials in an aqueous electrolyte consisting of 0.5 M CH_3OH and 0.1 M $HClO_4$ and normalizing the current density by the active surface area determined using H_{UPD} signals. Interestingly, all the examined Pt-RMA and Pt-HEA catalysts exhibit a significantly higher MOR area-specific current density than the Pt/C, indicating a promotion effect of these new catalysts on the intrinsic catalytic property. In particular, the Pt−Cr/C and Pt−Cr−Ta−V−Fe−Al/C exhibit current densities of 3.04 and 2.82 mA/cm_{Pt}^2, respectively, at 0.85 V versus RHE (Figure 6b), which correspond to more than threefold increase in comparison with the Pt/C (0.84 mA/cm_{Pt}^2). Benefiting from this significant increase in the intrinsic activity, the Pt−Cr−Ta−Fe−Al/C exhibits a slightly higher MOR mass activity than the Pt/C (204 mA/mg_{Pt} versus 198 mA/mg_{Pt}) at 0.85 V versus RHE even with a significantly smaller catalyst surface. Previous studies have revealed that MOR on many Pt−transition metal alloys follows the bifunctional catalysis mechanism.[40−42] Dissociative adsorption of methanol takes place on the Pt active sites. Oxygen-containing species such as water gets absorbed and activated on the adjacent transition metal sites, supplying oxygen-containing species OH_{abs}. These OH_{abs} can effectively interact with poisoning CO_{abs} intermediates generated on the Pt sites and facilitate their oxidation, resulting in the promoted MOR kinetics.[41,42] It is likely that Pt-RMA catalyzes MOR following

https://doi.org/10.1021/acs.chemmater.1c03389
Chem. Mater. 2022, 34, 266−272

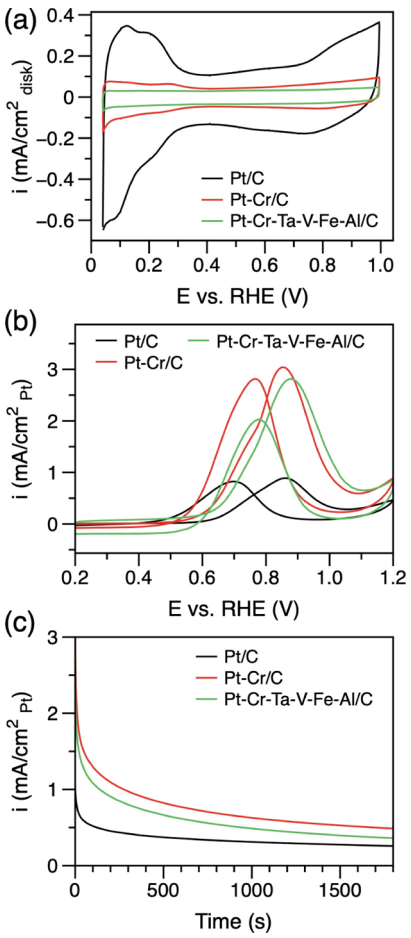

Figure 6. (a) CV curves of Pt−Cr/C, Pt−Cr−Ta−Fe−Al/C, and commercial Pt/C catalysts in N_2-purged 0.1 M $HClO_4$ electrolyte and (b) CV and (c) chronoamperometry curves of the three catalysts in MOR. The electrolyte consists of N_2-purged 0.1 M $HClO_4$ and 0.5 M CH_3OH aqueous solution.

the same bifunctional mechanism, thus exhibiting considerable activity improvement compared to monometallic Pt. Besides, the incorporation of reactive metal atoms separates the Pt active site ensembles and lowers the d-band center of the catalyst, which would help to weaken CO_{abs} adsorption strength and alleviate the CO_{abs} poisoning effect.[43] As a result, the Pt−Cr/C and Pt−Cr−Ta−V−Fe−Al/C retain a higher MOR activity in the catalyst durability test (Figure 6c).

CONCLUSIONS

In summary, a variety of Pt-RMA and Pt-HEA nanoparticles, including $Pt_{53}Cr_{47}$, $Pt_{56}Ta_{44}$, $Pt_{69}V_{31}$, $Pt_{71}Fe_{29}$, $Pt_{72}Al_{28}$, and $Pt_{28}Cr_{20}Ta_{20}V_{11}Fe_{11}Al_{10}$, were successfully prepared under ambient conditions using a hydrogen cold plasma synthesis method, demonstrating effectiveness, robustness, and universality of this new method for reducing reactive metals and alloys. The reduction of Pt-RMAs and Pt-HEAs is attributed to the generation of hydrogen anions in hydrogen plasma, which possess extremely strong reducing ability that allows simultaneous reduction of Pt and reactive metal precursors into nanoalloys. All the products are in the form of spherical nanoparticles of about 10 nm in size, with the alloy formation confirmed with XRD, XPS, and EDX elemental mapping characterizations. The obtained Pt-RMA and Pt-HEA nanoparticles were studied in MOR and demonstrate interesting catalytic properties. Particularly, the $Pt_{53}Cr_{47}/C$ and $Pt_{28}Cr_{20}Ta_{20}V_{11}Fe_{11}Al_{10}/C$ exhibit current densities of 3.04 and 2.82 mA/cm_{Pt}^2, respectively, at 0.85 V versus RHE, representing over threefold increase in the intrinsic activity compared with the commercial Pt/C catalyst. This study, by demonstrating the effectiveness of hydrogen cold plasma synthesis for overcoming the challenges encountered by conventional synthesis methods, provides a promising, universal strategy for making Pt-RMA and Pt-HEA nanoparticles and investigating for their new catalytic applications.

EXPERIMENTAL SECTION

Materials and Chemicals. Metal precursors, including chloroplatinic acid hydrate(IV) (≥99.9% trace metal basis), potassium tetrachloroplatinate(II) (≥99.9% trace metal basis), chromium(III) chloride hexahydrate (≥96%), tantalum(V) chloride (≥99.9% trace metal basis), vanadium(II) chloride (85%), iron(II) chloride tetrahydrate (≥99%), and aluminum(III) chloride (anhydrous, powder, 99.999% trace metal basis) were purchased from Sigma-Aldrich. Tantalum(V) chloride and aluminum(III) chloride were stored and handled in a nitrogen-filled glovebox due to their hygroscopic nature.

Synthesis of Pt−Cr, Pt−V, and Pt−Fe. In a typical synthesis of Pt−Cr alloy nanoparticles, 51.8 mg (0.1 mmol) of $H_2PtCl_6{\cdot}6H_2O$ and 26.6 mg (0.1 mmol) of $CrCl_3{\cdot}6H_2O$ were dissolved in 1 mL of deionized water. The solution was transferred to a vacuum oven and kept in vacuum at 70 °C overnight. After water and moisture were removed, the well-mixed precursors were collected and loaded into a custom-built DBD reactor. Ar gas was used to purge the DBD reactor for 20 min. Then, Ar gas was switched to H_2 gas for another 15 min. After that, the precursors were treated with H_2 cold plasma at atmospheric pressure for a total of 10 min. The input power of the plasma generator was kept at 90 W. After the plasma treatment, the material was collected and washed with deionized water three times. The as-synthesized Pt−Cr alloy was washed with 0.5 M H_2SO_4 overnight to remove the surface oxidation layer before any characterization. For the synthesis of Pt−V and Pt−Fe, the same procedure was used except for different metal precursors, which were VCl_2 and $FeCl_2{\cdot}4H_2O$.

Synthesis of Pt−Ta and Pt−Al. In a typical synthesis of Pt−Ta alloy nanoparticles, 51.8 mg (0.1 mmol) of $H_2PtCl_6{\cdot}6H_2O$ and 35.8 mg (0.1 mmol) of $TaCl_5$ were dissolved in 1 mL of ethanol. Ethanol was used instead of deionized water due to the hydrolysis reaction of $TaCl_5$. The rest of the material preparation and the following plasma treatment were the same as for Pt−Cr alloy. After the plasma treatment, the material was collected and washed with ethanol three times. The as-synthesized Pt−Ta alloy was washed by 0.5 M H_2SO_4 overnight to remove the surface oxidation layer before any characterization. The Pt−Al was synthesized the same way using $AlCl_3$.

Synthesis of Pt−Cr−Ta−V−Fe−Al. A total of 41.5 mg (0.1 mmol) of K_2PtCl_4, 26.6 mg (0.1 mmol) of $CrCl_3{\cdot}6H_2O$, 35.8 mg (0.1 mmol) of $TaCl_5$, 12.2 mg (0.1 mmol) of VCl_2, 19.9 mg (0.1 mmol) of $FeCl_3{\cdot}4H_2O$, and 13.3 mg (0.1 mmol) of $AlCl_3$ were mixed in a mortar. A pestle was used to apply force until the precursors were well-mixed. The mixture was transferred to a vacuum oven to remove possible moisture. Then, it was loaded into the DBD reactor, and the rest of the treatment was the same as for the Pt−Cr alloy.

Characterization. XRD patterns were acquired on a Bruker AXS Dimension D8 X-ray diffractometer with a Cu Kα radiation source. XPS was conducted on a PHI VersaProbe II scanning XPS microscope in ultrahigh vacuum. TEM was performed on a JEOL JEM-1230 microscope operated at 120 kV. HRTEM and STEM were performed on an FEI Tecnai G2 F20 microscope operated at 200 kV. SEM with EDX analysis was carried out on a Hitachi TM3030PLUS equipment with an operating voltage of 25 kV.

Electrode Preparation. Before the preparation of catalyst inks, metal alloy nanoparticles (Pt-M) were first mixed with Vulcan XC72

https://doi.org/10.1021/acs.chemmater.1c03389
Chem. Mater. 2022, 34, 266−272

carbon with 50 weight % catalyst loading. The mixture was well-dispersed in deionized water for 1 h. The dispersion was then centrifuged and dried overnight to obtain 50% Pt-M/C. A solution was prepared by mixing deionized water, isopropanol, and Nafion ionomer (volume ratio: $V_{water}/V_{isopropanol}/V_{Nafion}$ = 150:100:1). The catalyst inks were prepared by dispersing 4 mg of 50% Pt-M/C catalyst in 4 mL of prepared solution (1 mg catalyst/mL) and sonicated for 30 min. After that, 10 μL of catalyst ink was transferred dropwise onto a polished glass carbon rotating disk electrode (RDE, 0.196 cm^2) that was premounted on a custom-built rotating unit. The electrode was spun at 300 rpm and dried under gentle warm airflow for 10 min until a uniform thin catalyst film formed on the electrode (loading: 51 $\mu g_{catalyst}/cm^2$, 25 $\mu g_{Pt}/cm^2$).

Electrochemical Measurement. A CHI (CH Instruments, Inc.) 760D electrochemical workstation was used for electrochemical measurements. A standard three-electrode system was used, including a catalyst-coated glassy carbon as the working electrode, a platinum wire as the counter electrode, and a reversible hydrogen electrode (HydroFlex RHE, Gaskatel GmbH) as the reference electrode. The reversible hydrogen electrode was calibrated against a home-made hydrogen electrode. The CV curves were recorded in a N_2-purged aqueous electrolyte containing 0.1 M $HClO_4$ at room temperature, in the range of 0.04−1.00 V versus RHE at a scan rate of 50 mV/s. A total of 10 or more cycles of CV scan were recorded until the CV curves were stabilized. The methanol oxidation experiments were conducted in a N_2-purged electrolyte containing 0.1 M $HClO_4$ and 0.5 M CH_3OH.

Electrochemically Active Surface Area Measurement. The total charge of H adsorption was evaluated by integrating the area of the hydrogen under-potential deposition (H_{UPD}) in the recorded CV curve from 0.04 to 0.40 V. The electrochemically active surface area (ECSA) was calculated using the formula $ECSA = Q_H/(m_{Pt}\cdot q)$, $Q_H = \int_{E_1}^{E_2} i dV/S$, where Q_H is the total charge related to H adsorption, m_{Pt} is the active mass of the Pt catalyst on the RDE, q is the density of charge transfer during hydrogen adsorption (210 $\mu C/cm^2$ for polycrystalline Pt), i is the current, V is the potential, and S is the scanning rate.

■ ASSOCIATED CONTENT

Supporting Information

The Supporting Information is available free of charge at https://pubs.acs.org/doi/10.1021/acs.chemmater.1c03389.

Photographs of the experimental setup and prepared samples; TEM images of synthesized Pt−Cr, Pt−Ta, Pt−V, Pt−Fe, Pt−Al, and Pt−Cr−Ta−V−Fe−Al nanoparticles; SEM−EDX spectra of synthesized nanoparticles; alloy composition of Pt−Cr catalysts with different precursor feeding ratios; XPS spectra of metal elements in both metal precursors and synthesized alloy nanoparticles; XRD spectrum of the HEA nanoparticles; and CV and CA curves of all synthesized catalysts in an acidic electrolyte for MOR (PDF)

■ AUTHOR INFORMATION

Corresponding Author

Zhenmeng Peng − *Department of Chemical, Biomolecular, and Corrosion Engineering, The University of Akron, Akron, Ohio 44325, United States;* orcid.org/0000-0003-1230-6800; Email: zpeng@uakron.edu

Authors

Dezhen Wu − *Department of Chemical, Biomolecular, and Corrosion Engineering, The University of Akron, Akron, Ohio 44325, United States*

Libo Yao − *Department of Chemical, Biomolecular, and Corrosion Engineering, The University of Akron, Akron, Ohio 44325, United States*

Michael Ricci − *Department of Chemical, Biomolecular, and Corrosion Engineering, The University of Akron, Akron, Ohio 44325, United States*

Jialu Li − *Department of Chemical, Biomolecular, and Corrosion Engineering, The University of Akron, Akron, Ohio 44325, United States*

Rongxuan Xie − *Department of Chemical, Biomolecular, and Corrosion Engineering, The University of Akron, Akron, Ohio 44325, United States*

Complete contact information is available at: https://pubs.acs.org/10.1021/acs.chemmater.1c03389

Author Contributions

D.W. conducted the material synthesis and electrochemical test, analyzed the data, and drafted the original manuscript. L.Y. and M.R. offered insights about the plasma reactor setup and contributed to the material synthesis. J.l. and R.X. provided discussion and validation about the experiments. Z.P. conceived the idea, supervised the experiments, and edited the manuscript.

Notes

The authors declare no competing financial interest.

■ ACKNOWLEDGMENTS

The financial support of this work by the National Science Foundation (1955452) is acknowledged. HRTEM imaging was performed at the (cryo)TEM facility at the Liquid Crystal Institute, Kent State University, supported by the Ohio Research Scholars Program Research Cluster on Surfaces in Advanced Materials. The authors thank Dr. Min Gao for technical support with the TEM experiments.

■ REFERENCES

(1) Wang, C.; Li, D.; Chi, M.; Pearson, J.; Rankin, R. B.; Greeley, J.; Duan, Z.; Wang, G.; Van der Vliet, D.; More, K. L.; Markovic, N. M.; Stamenkovic, V. R.; More, K. L. Rational Development of Ternary Alloy Electrocatalysts. *J. Phys. Chem. Lett.* **2012**, *3*, 1668−1673.

(2) Wu, J.; Yang, H. Platinum-Based Oxygen Reduction Electrocatalysts. *Acc. Chem. Res.* **2013**, *46*, 1848−1857.

(3) Adzic, R. R. Platinum Monolayer Electrocatalysts: Tunable Activity, Stability, and Self-Healing Properties. *Electrocatalysis* **2012**, *3*, 163−169.

(4) Bing, Y.; Liu, H.; Zhang, L.; Ghosh, D.; Zhang, J. Nanostructured Pt-Alloy Electrocatalysts for PEM Fuel Cell Oxygen Reduction Reaction. *Chem. Soc. Rev.* **2010**, *39*, 2184−2202.

(5) Liu, Z.; Ma, L.; Zhang, J.; Hongsirikarn, K.; Goodwin, J. G., Jr. Pt Alloy Electrocatalysts for Proton Exchange Membrane Fuel Cells: A Review. *Catal. Rev.* **2013**, *55*, 255−288.

(6) Antolini, E.; Salgado, J. R. C.; Gonzalez, E. R. The Methanol Oxidation Reaction on Platinum Alloys with the First Row Transition Metals: The Case of Pt−Co and−Ni Alloy Electrocatalysts for DMFCs: A Short Review. *Appl. Catal., B* **2006**, *63*, 137−149.

(7) Tian, X. L.; Wang, L.; Deng, P.; Chen, Y.; Xia, B. Y. Research Advances in Unsupported Pt-Based Catalysts for Electrochemical Methanol Oxidation. *J. Energy Chem.* **2017**, *26*, 1067−1076.

(8) Debe, M. K. Electrocatalyst Approaches and Challenges for Automotive Fuel Cells. *Nature* **2012**, *486*, 43−51.

(9) Huang, X.; Zhao, Z.; Cao, L.; Chen, Y.; Zhu, E.; Lin, Z.; Li, M.; Yan, A.; Zettl, A.; Wang, Y. M.; Duan, X.; Mueller, T.; Huang, Y. High-Performance Transition Metal−Doped Pt3Ni Octahedra for Oxygen Reduction Reaction. *Science* **2015**, *348*, 1230−1234.

(10) Wu, D.; Shen, X.; Pan, Y.; Yao, L.; Peng, Z. Platinum Alloy Catalysts for Oxygen Reduction Reaction: Advances, Challenges and Perspectives. *ChemNanoMat* **2020**, *6*, 32−41.
(11) Peera, S. G.; Lee, T. G.; Sahu, A. K. Pt-Rare Earth Metal Alloy/Metal Oxide Catalysts for Oxygen Reduction and Alcohol Oxidation Reactions: An Overview. *Sustainable Energy Fuels* **2019**, *3*, 1866−1891.
(12) Greeley, J.; Stephens, I. E. L.; Bondarenko, A. S.; Johansson, T. P.; Hansen, H. A.; Jaramillo, T. F.; Rossmeisl, J.; Chorkendorff, I.; Nørskov, J. K. Alloys of Platinum and Early Transition Metals as Oxygen Reduction Electrocatalysts. *Nat. Chem.* **2009**, *1*, 552−556.
(13) Hu, Y.; Jensen, J. O.; Cleemann, L. N.; Brandes, B. A.; Li, Q. Synthesis of Pt−Rare Earth Metal Nanoalloys. *J. Am. Chem. Soc.* **2019**, *142*, 953−961.
(14) Liu, Y.; Chi, M.; Mazumder, V.; More, K. L.; Soled, S.; Henao, J. D.; Sun, S. Composition-Controlled Synthesis of Bimetallic PdPt Nanoparticles and Their Electro-Oxidation of Methanol. *Chem. Mater.* **2011**, *23*, 4199−4203.
(15) Brandiele, R.; Durante, C.; Grądzka, E.; Rizzi, G. A.; Zheng, J.; Badocco, D.; Centomo, P.; Pastore, P.; Granozzi, G.; Gennaro, A. One Step Forward to a Scalable Synthesis of Platinum−Yttrium Alloy Nanoparticles on Mesoporous Carbon for the Oxygen Reduction Reaction. *J. Mater. Chem. A* **2016**, *4*, 12232−12240.
(16) Itahara, H.; Takatani, Y.; Takahashi, N.; Kosaka, S. Sodium Vapor-Induced Synthesis of Intermetallic Pt5Ce Compound Nanoparticles. *Inorg. Chem.* **2020**, *59*, 13583−13588.
(17) Kanady, J. S.; Leidinger, P.; Haas, A.; Titlbach, S.; Schunk, S.; Schierle-Arndt, K.; Crumlin, E. J.; Wu, C. H.; Alivisatos, A. P. Synthesis of Pt3Y and Other Early−Late Intermetallic Nanoparticles by Way of a Molten Reducing Agent. *J. Am. Chem. Soc.* **2017**, *139*, 5672−5675.
(18) Furukawa, S.; Komatsu, T. Intermetallic Compounds: Promising Inorganic Materials for Well-Structured and Electronically Modified Reaction Environments for Efficient Catalysis. *ACS Catal.* **2017**, *7*, 735−765.
(19) Jong Yoo, S.; Kim, S.-K.; Jeon, T.-Y.; Jun Hwang, S.; Lee, J.-G.; Lee, S.-C.; Lee, K.-S.; Cho, Y.-H.; Sung, Y.-E.; Lim, T.-H. Enhanced Stability and Activity of Pt−Y Alloy Catalysts for Electrocatalytic Oxygen Reduction. *Chem. Commun.* **2011**, *47*, 11414−11416.
(20) Velázquez-Palenzuela, A.; Masini, F.; Pedersen, A. F.; Escudero-Escribano, M.; Deiana, D.; Malacrida, P.; Hansen, T. W.; Friebel, D.; Nilsson, A.; Stephens, I. E. L. The Enhanced Activity of Mass-Selected PtxGd Nanoparticles for Oxygen Electroreduction. *J. Catal.* **2015**, *328*, 297−307.
(21) Lindahl, N.; Eriksson, B.; Grönbeck, H.; Lindström, R. W.; Lindbergh, G.; Lagergren, C.; Wickman, B. Fuel Cell Measurements with Cathode Catalysts of Sputtered Pt3Y Thin Films. *ChemSusChem* **2018**, *11*, 1438−1445.
(22) Johansson, T. P.; Ulrikkeholm, E. T.; Hernandez-Fernandez, P.; Malacrida, P.; Hansen, H. A.; Bandarenka, A. S.; Nørskov, J. K.; Rossmeisl, J.; Stephens, I. E. L.; Chorkendorff, I. Pt Skin versus Pt Skeleton Structures of Pt 3 Sc as Electrocatalysts for Oxygen Reduction. *Top. Catal.* **2014**, *57*, 245−254.
(23) Pandey, A.; Mukherjee, D.; Borah, D.; Bandyopadhyay, M.; Tyagi, H.; Yadav, R.; Chakraborty, A. Characterization of Hydrogen Plasma in a Permanent Ring Magnet Based Helicon Plasma Source for Negative Ion Source Research. *Plasma Phys. Controlled Fusion* **2019**, *61*, 065003.
(24) Santoso, J.; Manoharan, R.; O'Byrne, S.; Corr, C. S. Negative Hydrogen Ion Production in a Helicon Plasma Source. *Phys. Plasmas* **2015**, *22*, 093513.
(25) Kakati, B.; Kausik, S. S.; Bandyopadhyay, M.; Saikia, B. K.; Kaw, P. K. Development of a Novel Surface Assisted Volume Negative Hydrogen Ion Source. *Sci. Rep.* **2017**, *7*, 11078.
(26) Di, L.; Zhang, J.; Zhang, X. A review on the recent progress, challenges, and perspectives of atmospheric-pressure cold plasma for preparation of supported metal catalysts. *Plasma Processes Polym.* **2018**, *15*, 1700234.
(27) Qi, B.; Di, L.; Xu, W.; Zhang, X. Dry Plasma Reduction to Prepare a High Performance Pd/C Catalyst at Atmospheric Pressure for CO Oxidation. *J. Mater. Chem. A* **2014**, *2*, 11885−11890.
(28) Di, L. B.; Duan, D. Z.; Park, D.-W.; Ahn, W.-S.; Lee, B.-J.; Zhang, X. L. Cold Plasma for Synthesizing High Performance Bimetallic PdCu Catalysts: Effect of Reduction Sequence and Pd/Cu Atomic Ratios. *Top. Catal.* **2017**, *60*, 925−933.
(29) Liu, C.; Li, M.; Wang, J.; Zhou, X.; Guo, Q.; Yan, J.; Li, Y. Plasma Methods for Preparing Green Catalysts: Current Status and Perspective. *Chin. J. Catal.* **2016**, *37*, 340−348.
(30) Cheng, X.; Dong, P.; Huang, Z.; Zhang, Y.; Chen, Y.; Nie, X.; Zhang, X. Green Synthesis of Plasmonic Ag Nanoparticles Anchored TiO2 Nanorod Arrays Using Cold Plasma for Visible-Light-Driven Photocatalytic Reduction of CO2. *J. CO_2 Util.* **2017**, *20*, 200−207.
(31) Sun, Y.; Dai, S. High-Entropy Materials for Catalysis: A New Frontier. *Sci. Adv.* **2021**, *7*, No. eabg1600.
(32) Yao, Y.; Huang, Z.; Xie, P.; Lacey, S. D.; Jacob, R. J.; Xie, H.; Chen, F.; Nie, A.; Pu, T.; Rehwoldt, M.; Yu, D.; Zachariah, M. R.; Wang, C.; Shahbazian-Yassar, R.; Li, J.; Hu, L. Carbothermal Shock Synthesis of High-Entropy-Alloy Nanoparticles. *Science* **2018**, *359*, 1489−1494.
(33) Toshifuji, J.; Katsumata, T.; Takikawa, H.; Sakakibara, T.; Shimizu, I. Cold Arc-Plasma Jet under Atmospheric Pressure for Surface Modification. *Surf. Coat. Technol.* **2003**, *171*, 302−306.
(34) Laroussi, M.; Akan, T. Arc-free Atmospheric Pressure Cold Plasma Jets: A Review. *Plasma Processes Polym.* **2007**, *4*, 777−788.
(35) Escudero-Escribano, M.; Malacrida, P.; Hansen, M. H.; Vej-Hansen, U. G.; Velazquez-Palenzuela, A.; Tripkovic, V.; Schiotz, J.; Rossmeisl, J.; Stephens, I. E. L.; Chorkendorff, I. Tuning the Activity of Pt Alloy Electrocatalysts by Means of the Lanthanide Contraction. *Science* **2016**, *352*, 73−76.
(36) Bardi, U.; Beard, B. C.; Ross, P. N. Surface Oxidation of a Pt−20% CO Alloy: An X-ray Photoelectron Spectroscopy and Low-energy Electron Diffraction Study on the [100] and [111] Oriented Single-crystal Surfaces. *J. Vac. Sci. Technol., A* **1988**, *6*, 665−670.
(37) Wood, G. C.; Stott, F. H. Oxidation of Alloys. *Mater. Sci. Technol.* **1987**, *3*, 519−530.
(38) Osei-Agyemang, E.; Balasubramanian, G. Surface Oxidation Mechanism of a Refractory High-Entropy Alloy. *npj Mater. Degrad.* **2019**, *3*, 20.
(39) Zhao, Y.; Wu, Y.; Liu, J.; Wang, F. Dependent Relationship between Quantitative Lattice Contraction and Enhanced Oxygen Reduction Activity over Pt−Cu Alloy Catalysts. *ACS Appl. Mater. Interfaces* **2017**, *9*, 35740−35748.
(40) Antolini, E. Pt-Ni and Pt-M-Ni (M = Ru, Sn) Anode Catalysts for Low-Temperature Acidic Direct Alcohol Fuel Cells: A Review. *Energies* **2017**, *10*, 42.
(41) Spendelow, J. S.; Wieckowski, A. Electrocatalysis of Oxygen Reduction and Small Alcohol Oxidation in Alkaline Media. *Phys. Chem. Chem. Phys.* **2007**, *9*, 2654−2675.
(42) Zhao, X.; Yin, M.; Ma, L.; Liang, L.; Liu, C.; Liao, J.; Lu, T.; Xing, W. Recent Advances in Catalysts for Direct Methanol Fuel Cells. *Energy Environ. Sci.* **2011**, *4*, 2736−2753.
(43) Huang, H.; Hu, X.; Zhang, J.; Su, N.; Cheng, J. Facile Fabrication of Platinum-Cobalt Alloy Nanoparticles with Enhanced Electrocatalytic Activity for a Methanol Oxidation Reaction. *Sci. Rep.* **2017**, *7*, 45555.

https://doi.org/10.1021/acs.chemmater.1c03389
Chem. Mater. 2022, 34, 266−272